TECHNICAL REPORT

A plasma irradiation system optimized for space weathering of solar system bodies

Tomoki Kimura[1*], Misako Otsuki[1†], Tomohiro Kitano[1†], Ryo Hoshino[1†], Yusuke Nakauchi[2], Shunsuke Haganuma[3], Ryu Haganuma[3], Tetsuo Haganuma[3], Fuminori Tsuchiya[4], Toru Tamagawa[5], Asami Hayato[6], Jun Kimura[7], Naoki Terada[4], Hideyuki Usui[8], Masaki N. Nishino[9], Shoichiro Yokota[7] and Yohei Miyake[8]

Abstract

In the tenuous atmospheric bodies of our solar system, space weathering on the celestial surface is an important process for its chemical and physical evolution and ambient environment on timescales of celestial evolution. Space plasma is a dominant energy and material source for space weathering. Plasma irradiation experiment in the laboratory is an effective method for modeling space weathering driven by space plasma. However, comprehensive modeling of plasma space weathering has not yet been conducted because the capabilities of the earlier facilities were not optimized for realistic space weathering; for example, the incident electron and ion were not irradiated in the same condition. Here, we developed a plasma irradiation system, Plasma Irradiation Emulator for Celestial Environments (PIECE) of the solar system bodies, which reproduces plasma space weathering in tenuous atmospheric bodies by the electron and ion irradiations in the same condition. We successfully developed a system with high electron and ion number fluxes of $\sim 10^{13} - 10^{16}$ particles $cm^{-2}s^{-1}$ at any acceleration energy in the range of 1–30 keV, which leads to a fluence of e.g., $\sim 10^{18} - 10^{21}$ particles $cm^{-2}s^{-1}$, with a 1-day irradiation time. This fluence corresponds to a plasma irradiation time of $\sim 10^3 – 10^6$ years on Europa.

[†]Misako Otsuki, Tomohiro Kitano and Ryo Hoshino have contributed equally to this work.

*Correspondence:
Tomoki Kimura
kimura@rs.tus.ac.jp
Full list of author information is available at the end of the article

Graphical Abstract
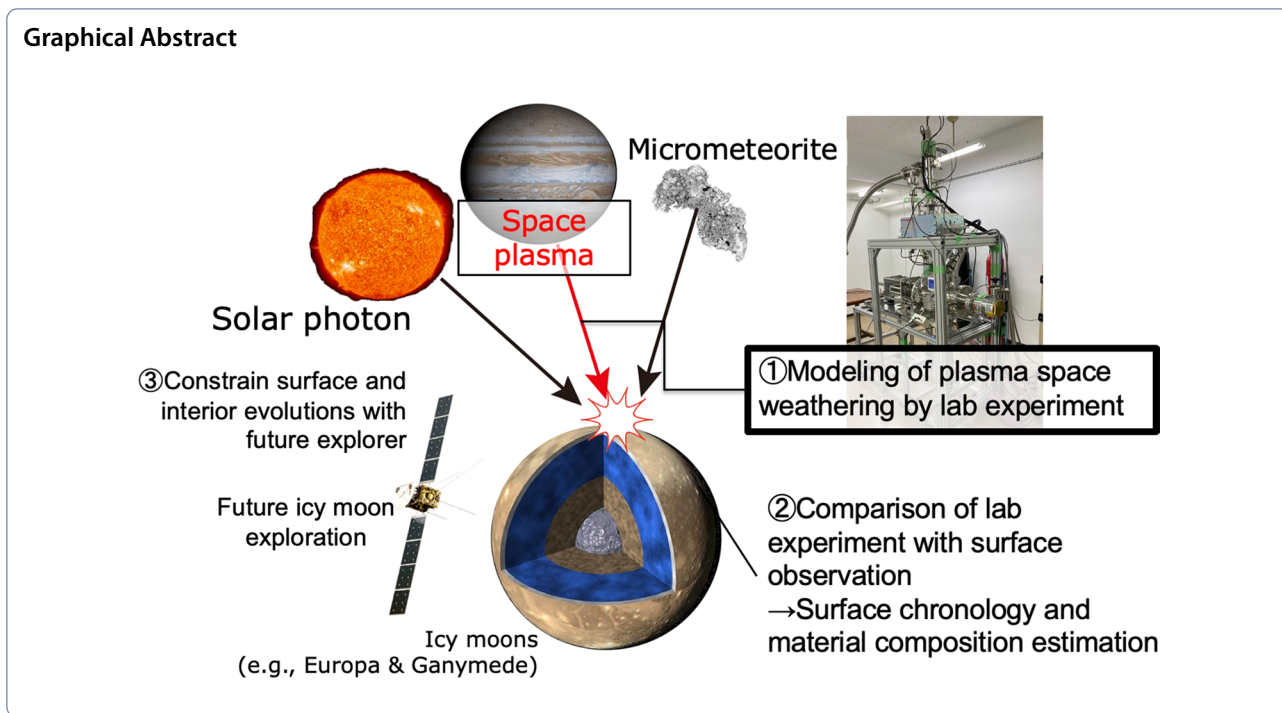
Introduction

In our solar system, planets, moons, and small bodies interact with the ambient space through a variety of physical and chemical processes. The solar system bodies are irradiated with the solar wind, planetary plasmas, cosmic rays, solar photons, and micrometeorites. The materials of the atmosphere and/or solid surface of the bodies are altered through physical and chemical processes, such as sputtering, ionization, dissociation, and implantation of the incident particles. These material alterations are known as space weathering (Johnson 1990; Johnson et al. 2004; Bennett et al. 2013; Pieters and Noble 2016). Each type of incident particle and photon has different physical and chemical effects on the atmospheric and surface materials. For example, solar wind and planetary plasma ions sputter atoms and molecules from the surface and atmospheric materials, accompanied by the destruction of the molecular structure of the materials. This is known as amorphization if the irradiated materials have a crystal structure (Laczniak et al. 2021). The sputtered atoms and molecules create a tenuous atmosphere (Ip et al. 1998). The incident ions and electrons ionize and dissociate atoms and molecules in the irradiated materials, creating secondary electrons. New chemical compounds are synthesized through reactions associated with dissociated atoms and molecules. These non-thermal processes are dominantly driven by planetary plasmas, cosmic rays, solar wind, and solar photons at X-ray and ultraviolet (UV) wavelengths (e.g., Bennett et al. 2013 and references therein). Contrarily, the solar photons at the visible and infrared wavelengths contribute less to the non-thermal effects but work as thermal energy sources that drive the thermal desorption of atoms and molecules from the surface and atmosphere (Madey et al. 1998). Micrometeoroid bombardment on the solid surface vaporizes the surface material, followed by vitrification of the surface material and turnover of the surface regolith layer through shock wave formation, as implied from laboratory experiments of laser irradiation (Sasaki et al. 2001; Moroz et al. 2014).

In the solar system bodies with tenuous atmospheres (e.g., Mercury, Moon, Martian moon Phobos, icy moons of the gas giants, asteroids, and other small bodies), the incident particles and photons precipitating from space directly reach the solid surface with less atmospheric absorption compared to those precipitating to the bodies with thick atmospheres. The surface material of a tenuous atmospheric body has long been processed through space weathering. For example, the crater chronology of the icy moons of Jupiter, which are Europa, Ganymede, and Callisto, indicated that the average age of their surfaces ranges from 10^7 (Europa) to 4×10^9 (Callisto) years old (Zahnle et al. 1998). This implies that the surface of the icy moons was exposed to space and is likely altered on timescales of celestial evolution, experiencing space weathering by the irradiation of the magnetospheric plasma, solar photons, and micrometeorites.

Kimura *et al. Earth, Planets and Space*   (2023) 75:150

Page 3 of 15

Carlson et al. (2009) summarized the atomic fluxes of micrometeorites and magnetospheric plasmas in Europa orbit. They showed that the oxygen atomic number flux originating from the magnetosphere has the greatest value of 3×10^8 atoms $m^{-2}s^{-1}$ in the particles precipitating to the surface of Europa. Based on in situ observations with the Galileo spacecraft at the icy moons of Jupiter, Cooper et al. (2001) estimated the energy fluxes of the magnetospheric plasma in the keV–MeV range and that of the solar photons from the extreme ultraviolet (EUV) to the infrared. On Europa, the plasma energy flux accessible to the surface (7.8×10^{10} keV cm^{-2}s^{-1}) was found to be greater than the solar UV-C photons at 4.4–12.4 keV (4.0×10^{10} keV cm^{-2}s^{-1}) that dissociate molecules in the surface material. As for the other icy moons, it was also found that the plasma energy flux on Ganymede and Callisto ($0.22\text{-}5.4 \times 10^9$ keV cm^{-2} s^{-1}) still has a non-negligible contribution to the energy input to the surface. These estimations indicate the dominant effect of the magnetospheric plasma of Jupiter on space weathering on the icy moon surface.

The earlier studies introduced above imply that plasma space weathering drives the chemical and physical evolution of surface materials in the icy moons of Jupiter (see also Johnson et al. 2004 for a more comprehensive discussion). Material processing by plasma irradiation is too complex to be described only by theory and/or telescope/spacecraft observations. The laboratory experiment of plasma irradiation is one of the most effective methods to unveil material processing because complex chemical and physical processes are realistically reproduced and analyzed in detail with on-site laboratory analysis facilities. Many earlier studies addressed plasma space weathering on the moons of Jupiter based on laboratory experiments of electron or ion irradiation (Nash and Fanale 1977; Nelson and Nash 1979; Johnson 1990; Johnson et al. 2004; Moore et al. 2007; Hand and Carlson 2015; Poston et al. 2017; Tribbett and Loeffler 2021). They specifically discussed the dissociation, sputtering, material oxidization, reflectance change, and others that occurred in the irradiated target samples that comprised model material for the icy moon surface (e.g., NaCl and water ice). However, their focus was on the specific pairs of incident particles and target materials (e.g., electron versus NaCl), which do not realistically reproduce the plasma space weathering on the icy moon surface, but in reality, the irradiation of both electrons and ions on the various materials in the same condition. If realistic space weathering is successfully reproduced by a laboratory experiment in the same condition for the incident ion and electron,

the chemical and physical surface evolutions can be unveiled. The surface evolution constrains the alteration histories of the seawater that is transported from the interior ocean to the surface, which potentially leads to the characterization of the chemical composition of the interior ocean.

Here, we present the development of a plasma irradiation system, the Plasma irradiation Emulator for Celestial Environments (PIECE) of the solar system bodies, which in the same condition reproduces plasma space weathering for both energetic electrons and ions in the icy moons of Jupiter and other solar system bodies. We successfully developed a system with electron and ion number fluxes of $\sim 10^{13} - 10^{16}$ particles cm^{-2} s^{-1} at any acceleration energy in the range of 1–30 keV, which corresponds to a fluence of e.g., $\sim 10^{18} - 10^{21}$ particles cm^{-2} with a 1-day irradiation time. This fluence is equivalent to a plasma irradiation time of $\sim 10^3$–10^6 years on Europa. It should be noted that the space weathering is not reproduced realistically for a too long period (e.g., up to 10^6 years on Europa) with the high fluence because of the greater laboratory particle flux compared to that around the target bodies, which might lead to the heating for the experiment sample. However, it is feasible for our laboratory experiment to investigate the dependence of space weathering on the incident particle flux keeping the same particle fluence. The incident flux dependence has not been investigated yet for both the incident ions and electrons in the same condition.

Our irradiation system is broadly applicable to tenuous atmospheric bodies in the solar system. For example, the system can reproduce space weathering on the surfaces of Mercury, the Moon, and asteroids driven by the solar wind hydrogen that forms water molecules from surface silicate minerals (Zhu et al. 2019; Nakauchi et al. 2021). On Mercury and the Moon, the created water molecules are likely to be accumulated as ice in the permanent shadow in the polar region (Jones et al. 2018, 2020). Our system is also applicable to the Moon and Phobos. Planetary atmospheric particles escape as the 'planetary wind' to space and are implanted into the soils of their moons (Ozima et al. 2005; Terada et al. 2017). Reproducing the space weathering driven by solar and planetary winds with our irradiation system, we investigate the evolution of the surface environment, solar wind, planetary atmosphere, and celestial material origin.

In "System requirements"Section, the requirements for the PIECE system development are described. In "System overview" Section, we overview the function and operating principle of the system. In "Performance test results" Section, the results of the system performance test are presented.

Kimura *et al. Earth, Planets and Space*   (2023) 75:150

Page 4 of 15

System requirements

Table 1 summarizes the requirements of the PIECE system. All the requirements were successfully satisfied for the developed system.

The species of the incident particles are electrons, hydrogen, oxygen, helium, and carbon ions that comprise the planetary magnetospheric plasma, planetary atmosphere, and solar wind mainly in the form of the atomic ion. In the Jupiter system, the sulfur ion originating from the volcanoes of Io is also the main component of magnetospheric plasma, which is an important aspect of the irradiation system. However, the sulfur ion sources for irradiation are toxic gases, such as H_2S and SO_2. It is technically difficult to safely introduce them into the system and avoid the degradation of its components by the introduced gases. The sulfur ion is out of the scope for the present development and will be addressed in a future study. Recently, the Juno explorer discovered the water-group molecular ions, e.g., H_2^+ and O_2^+, around Jupiter's icy moons as well as Saturn's icy moons (Szalay et al. 2022; Valek et al. 2022). We include the irradiation of the water-group molecular ions for our scope of the present development.

The incident ions and electrons are accelerated to any energy in the range of 1–30 keV, which is one of the populations comprising the planetary magnetospheric plasma and solar wind. It should be noted that because of the technical constraint on the particle acceleration energy our system reproduces only a part (1–30 keV) of the broad spectral range of the magnetospheric and solar wind energetic particles that spans from keV to MeV (e.g., Mauk 2004). The energy of escaping planetary atmospheric particles depends on their location, but the in situ spacecraft measurement suggested that the energy of the escaping atmospheric particle distant from the planet is comparable with that of the magnetospheric plasma, for example, from 100s eV to 10s keV in Earth (Seki et al. 1998, 2001; Terada et al. 2017).

The number fluence of the incident particle needs to be 10^{18} particles cm^{-2} or greater, which is comparable to or greater than those of the typical values in earlier studies (Hand and Carlson 2015), to reproduce the space weathering on timescales longer than $\sim 10^2$ years on Europa. With a technically feasible flux of the incident particles, for example, $\sim 10^{13} - 10^{16}$ particles cm^{-2} s^{-1}, the irradiation time must be at least $10^2 - 10^5$ sec satisfy the minimum requirement for the number fluence. The required fluence is reasonably achieved with exclusive use, which is the novelty of our system. With these specifications, the dependence of space weathering on the incident particle flux can also be investigated changing the flux by a few orders of magnitude keeping the same fluence.

The minimum temperature of the target sample is 80–100 K, which is the typical surface temperature of the icy moons of Jupiter (e.g., Spencer et al. 1999). The target samples used for the irradiation experiment comprised various surface model materials for tenuous atmospheric bodies. Most surface materials are in powder form with a variety of particle sizes ranging from nanometers to millimeters (Helfenstein and Shepard 1999; Tsuchiyama et al. 2011). The target sample is in powder form, and the surface should be horizontal at the incident particle beam line to avoid the collapse of the sample.

System overview
Functional overview

Figure 1 presents a functional overview of the PIECE system. The main vacuum chamber has a cylindrical shape with a volume of 1.3×10^4 cm^3, whose axis is aligned horizontally. The chamber is evacuated

Table 1 Requirements for the PIECE system

| Item	Value	Comment
Particle species	Electron, H, O, He, C ions	The main components of the planetary magnetospheric plasmas, atmospheres, and solar wind. Include some molecular ions recently discovered around Jupiter's icy moons (e.g., H_2^+, O_2^+) as well as the typical atomic ions (e.g., H^+, O^+, C^+)
Particle energy	Any energy in a range of 1–30 keV	A population comprising the planetary magnetospheric plasma, escaping planetary atmospheric particles, and solar wind
Fluence	$> 10^{18}$ particles cm^{-2}	Greater than the typical value of e.g., $\sim 10^2$ years on Europa in earlier studies
Irradiation time	$> 10^2 - 10^5$ sec	Exclusive use, non-public facility
Sample temperature	80–300 K	From the typical surface temperature of Jupiter's icy moons (80–100 K) to the room temperature
Sample material	Salts (e.g., $MgSO_4$, NaCl), silicate minerals, etc., in powder, H_2O ice	The model material for the icy moon surface (Carlson et al. 2009), Mercury, Moon, asteroids, and other bodies (Nittler et al. 2011; Zhu et al. 2019; Nakauchi et al. 2021)
Sample mounting	Sample surface to be horizontal at the beamline	Avoid collapse of the powder sample
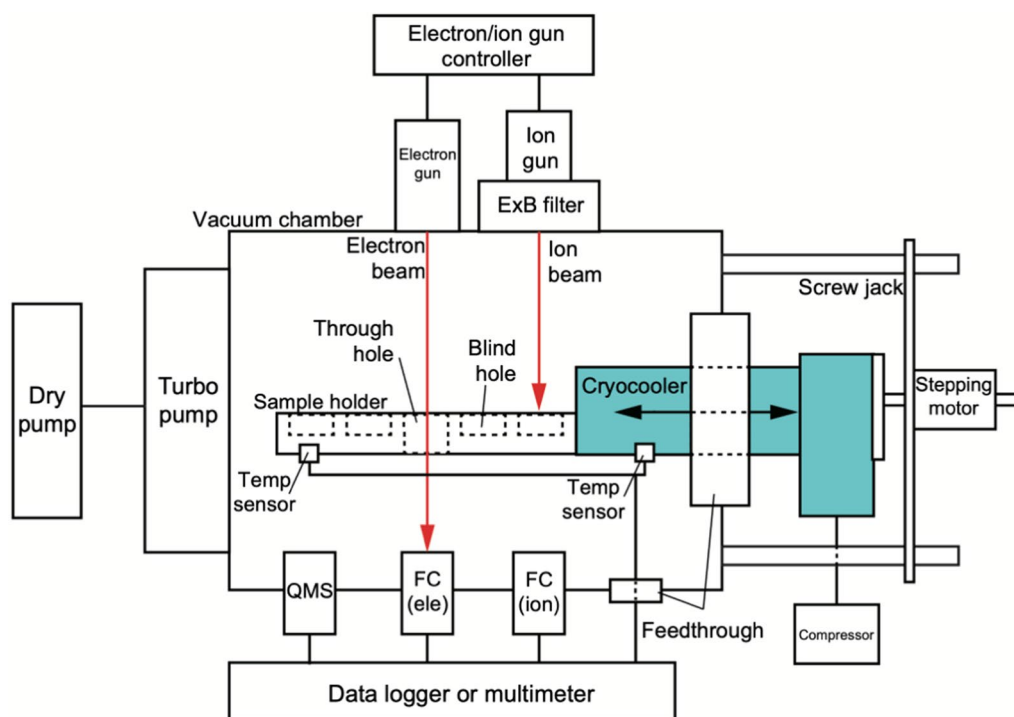
Fig. 1 Schematic representing the functional overview of the PIECE system

with a turbo molecular pump at an evacuation rate of $3.3 \times 10^5 \, \text{cm}^3\text{s}^{-1}$, which leads to a typical pressure of $\sim 10^{-6} - 10^{-5}$ Pa in the chamber. The sample holder, cryocooler (see "Sensors and cryocooler" Sect.), electron gun ("Electron gun" Sect.), ion gun with an $E \times B$ filter ("Ion gun with E x B filter" Sect.), and sensors ("Sensors and cryocooler" Sect.) are mounted in the main chamber. A copper sample holder is aligned with the cylinder axis of the main chamber and directly mounted on the cryocooler, which is cooled to ~ 100 K when no irradiation was performed. The temperatures at the tip and base of the sample holder are monitored using platinum resistance thermometers connected to the data logger. Through a vacuum feedthrough, the cryocooler is connected to the screw jack outside the chamber. The sample holder mounted on the cryocooler is moved horizontally with the screw jack actuated by the stepping motor. The electron gun and ion gun with an $E \times B$ filter are mounted at a working distance of 164 mm from the sample holder. The ion or electron beam is perpendicular to the sample holder. The blind hole or through hole in the sample holder is located at the ion or electron beam line by moving the sample holder. The target sample in the blind hole is irradiated with an electron gun or ion gun at the beamline. The beam current passing through the blind hole is measured with a Faraday cup (FC) mounted on the opposite side of the electron or ion gun in the main

chamber. The partial pressure of each particle degassed from the target sample and inner wall of the main chamber is monitored using a quadrupole mass spectrometer (QMS). The sample, sample cup, sample holder, and inner wall of the main chamber are all grounded to suppress the electrical charging of a sample. The secondary electrons (and possibly the secondary ions) emitted from the surface sample during the particle irradiation are immediately absorbed by the grounded components, which would significantly suppress the sample charging. The measurement of electromagnetic structure around the irradiated sample would be a good future work that we should address to unveil the particle acceleration/deceleration on the airless body surface, e.g., Moon (Saito et al. 2012). A photograph of the complete PIECE system is shown in Fig. 2.

Sensors and cryocooler

QMS is an MKS Macrovision-2 Residual Gas Analyzer with a mass range of 1–100 amu and detection sensitivity of $> 5 \times 10^{-12}$ Pa. The ion source sensor of QMS is located at a ~ 60 mm distance from the sample, which is exposed to the main cylindrical space of the main chamber. The FC for the electron or ion beam current measurement is an Omegatron OMS-0070FC with a beam aperture diameter of 20 mm, detection sensitivity of 10 nA, and dynamic range of 0–10 mA. The FC is
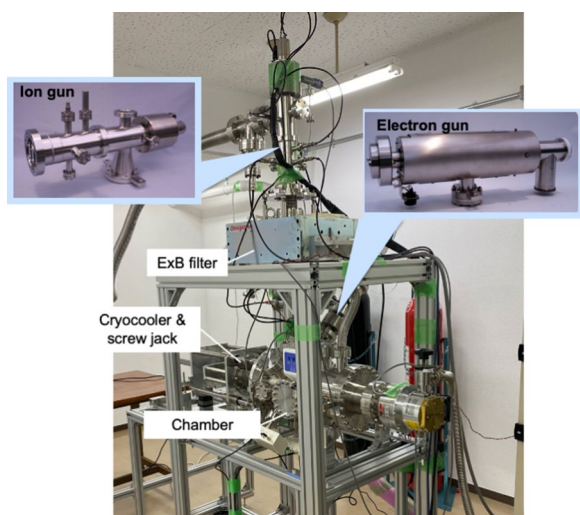
Kimura *et al. Earth, Planets and Space*   (2023) 75:150

Page 6 of 15

Fig. 2 A photograph showing the exterior of the developed PIECE system

Fig. 3 Schematic illustrating the operating principle of the electron gun implemented on the PIECE system

mounted at a working distance of approximately 320 mm from the ion or electron gun. The temperature sensor mounted on the sample holder is a NETSUSHIN Pt100 film thermometer with a dynamic range of ~70–370 K and a measurement uncertainty of 0.35 K at 100 K. The cryocooler is an ULVAC RMS50 with a C30VR compressor with a cooling power of 85 W at 77 K. The two-dimensional profile of the beam current diameter was measured only during the performance test. The profile monitor used is the Omegatron Current Profile Monitor OMS-0600PM with a beam aperture diameter of 0.5 mm, which is swept in the beam-perpendicular plane with a measurement interval of 1 mm in the x-axis direction and 0.002 mm in the y-axis direction (see "Other performances of ion gun" Sect.).

Sample analysis
The surface reflectance of the irradiated samples is analyzed with spectrometers to quantify the material alteration caused by the plasma space weathering. We are going to implement the Fourier transfer infrared (FTIR) spectrometer and ultraviolet–visible (UV–VIS) spectrometer for the vacuum reflectance measurements in the main chamber. The samples cooled with the cryocooler are going to be analyzed with the future vacuum spectrometry system. At present, the powder samples at room temperature are removed from the main chamber after irradiation, and their surface reflectance is measured in air with FTIR and UV–VIS spectrometers. Requirements for the reflectance analysis, e.g., wavelength, spectral resolution, and sensitivity, are defined based on the scientific purpose of each experiment.
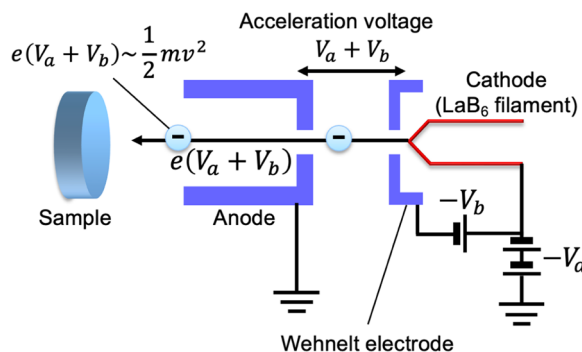
Electron gun
The electron gun implemented on the PIECE system is the Omegatron 30 keV LaB$_6$ electron gun (OME-3040LA). The beam energy ranges from 1 to 30 keV, with a beam diameter of 0.01–10 mm and a beam current of 1.9-2.5 mA at 10–30 keV. The details of the measured beam current are presented in "Electron gun" Section. Figure 3 illustrates the operating principle of the e-gun. Thermal electrons are emitted from the cathode of the LaB$_6$ filament at a voltage $-V_a < 0$. The emitted thermal electrons are accelerated toward the grounded anode. Between the anode and cathode, the Wehnelt electrode biased by a voltage $-V_b < 0$. from the filament voltage $-V_a$ is located to control the emission rate of the thermal electron. The effective acceleration voltage $V_a + V_b$. is associated with the kinetic energy of the accelerated electron:

$$e(V_a + V_b) \sim \frac{1}{2}mv^2, \tag{1}$$

where e, m, and v are the elementary charge, electron mass, and speed of the accelerated electrons, respectively. An accelerated electron beam is delivered to the target sample. Using Eq. 1, the beam energy is controlled by changing voltages V_a and V_b.

Ion gun with E x B filter
The ion gun with the $E \times B$ filter implemented on the PIECE system is an Omegatron cold cathode ion gun (OMI-0090). The beam energy ranges from 0.7 keV to 10 keV with a beam diameter of several millimeters and beam current of 10s μA at 10 keV. The details of the measured beam current are presented in "Ion gun" Section.

Figure 4 illustrates the operating principle of the implemented ion gun with an $E \times B$ filter. The ion source gas is filled into the discharge chamber, where temporally static
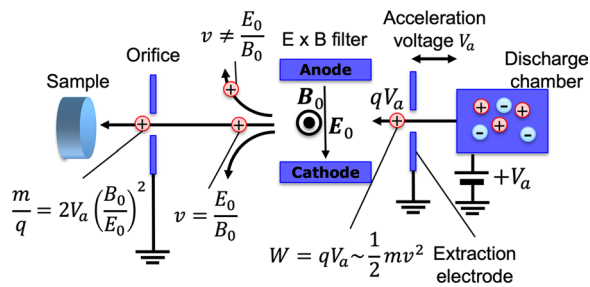
Fig. 4 Schematic illustrating the operating principle of the ion gun with the E x B filter implemented on the PIECE system

magnetic and electric fields are applied. Gas neutrals are ionized by collisions between electrically accelerated electrons/ions and gas neutrals, which create multiple species of ions from the gas neutrals. The created ions are trapped, and gyration starts in the applied magnetic field. An ion with charge q and mass m extracted from the discharge chamber charged at an acceleration voltage $V_a > 0$ is accelerated toward the grounded extraction electrode. Moving through the hole of the extraction electrode, the ion obtains kinetic energy:

$$qV_a \sim \frac{1}{2}\mathrm{m}v^2, \tag{2}$$

where v is the speed of the accelerated ion. In the $E \times B$ filter, temporally static and uniform magnetic and electric fields are applied between the anode and cathode of the capacitor. Ion at the speed of $E \times B$ drift:

$$v = \frac{E_0}{B_0}, \tag{3}$$

moves straight, while the ion at a speed $v \neq E_0/B_0$ deflects, where E_0 is the magnitude of the uniform electric field perpendicular to the uniform magnetic field with a flux density magnitude B_0 applied between the capacitor plates. In practice, electric and magnetic fields are created using capacitor plates and electromagnetic coils, respectively. The accelerated ion at a speed $v = E_0/B_0$ is collimated at the orifice and delivered to the target sample. From Eqs. 2, 3, the following relationship is obtained for the mass per charge ratio m/q of the filtered ion:

$$\frac{m}{q} = 2V_a \left(\frac{B_0}{E_0} \right)^2. \tag{4}$$

Accelerated ions with any desired mass per charge, m/q is extracted by changing V_a, E_0, and B_0. In nominal operation, V_a and E_0 are set to be constant, whereas B_0

is swept by changing the current of the electromagnetic coil to obtain ions with the desired m/q ratio.

The magnetic field B_0 in the $E \times B$ filter is not spatially uniform because it extends outside the region between capacitor plates. This weakens the magnetic flux density between capacitor plates. In the performance test, the effective magnetic flux density B_{eff} is measured between the capacitor plates with a tesla meter, which leads to the magnetic field efficiency ε that associates the theoretical magnetic flux $B_0 = E_0/v$ with B_{eff} with a relation $B_{\mathrm{eff}} = \varepsilon B_0$. Figure 5 shows the magnetic flux density B_{eff} measured between the capacitor plates with a tesla meter as a function of electromagnetic coil current.

Performance test results

Here, we describe the results of the system performance test performed using the configurations for the nominal irradiation experiment. We assessed the beam current of the electron/ion gun, mass per charge resolution of the $E \times B$ filter, and sensitivity of the QMS partial pressure. All assessments were performed at room temperature. The performance tests for the electron and ion guns in "Electron gun" and "Ion gun" Sections. were conducted without an irradiation sample mounted in the main chamber, while a NaCl sample was mounted in the chamber for the mass spectrometer test in "Mass spectrometer" Section.
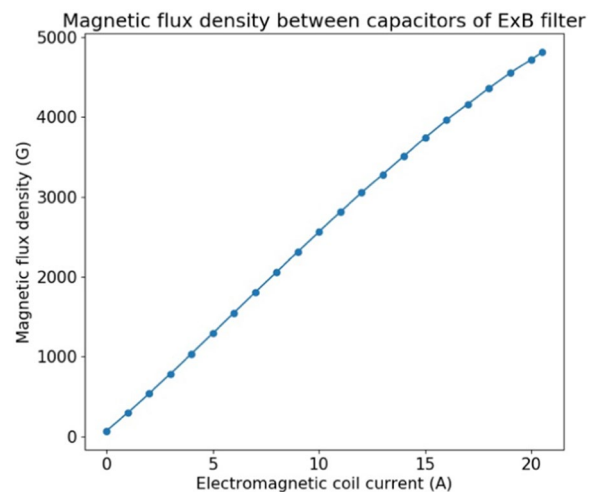

Fig. 5 Plot showing the magnetic flux density measured between capacitor plates of the $E \times B$ filter as a function of electromagnetic coil current

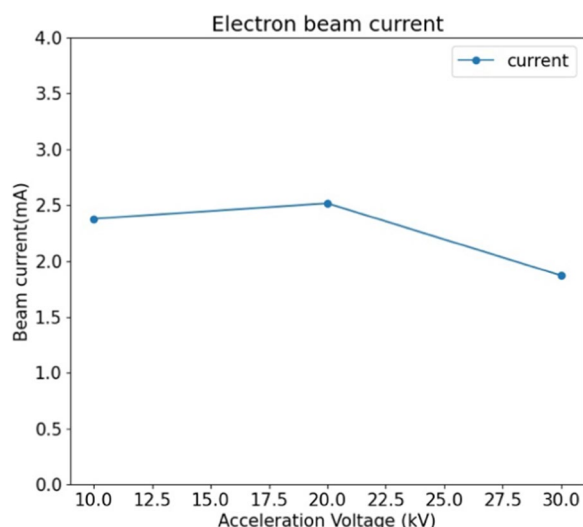Kimura *et al. Earth, Planets and Space*   (2023) 75:150

Page 8 of 15

Fig. 6 Plot showing the maximum electron beam current as a function of acceleration voltage. The blue line is the beam current in a unit of mA measured with FC

Electron gun

Figure 6 shows the electron beam current at 10−30 keV measured during the electron gun performance test. The blue line represents the beam current in units of mA measured with the FC. The maximum beam current ranges from 1.87 to 2.52 mA at 10−30 keV. For the irradiation experiment for the icy moon sample, the beam diameter is going to be defocused down to 10 mm to irradiate the pelletized powder sample in a copper cylinder cup with a diameter of ~ 11 mm and thickness of ~ 1.5 mm. The number and energy fluxes with a 10 mm-beam diameter were estimated to be $1.49 - 2.00 \times 10^{16}$ particles $cm^{-2}s^{-1}$, and $1.89 - 4.46 \times 10^{17}$ keV $cm^{-2}s^{-1}$, which are equivalent to the number and energy fluences of $1.28 - 1.73 \times 10^{21}$ particles cm^{-2}, and $1.63 - 3.85 \times 10^{22}$ keV cm^{-2}, with a 1-day irradiation time in the experiment, respectively. The obtained number fluence satisfies the system requirements defined in "System requirements" Section. With the number and energy fluxes $(1.8 \times 10^8$ particles $cm^{-2}s^{-1})$, and $(6.2 \times 10^{10}$ keV $cm^{-2}s^{-1})$, of the keV–MeV electrons measured with the Galileo explorer in the orbit of Europa (Cooper et al. 2001), the estimated number and energy fluences correspond to irradiation times of $2.3 - 3.0 \times 10^5$ year and $0.84 - 2.0 \times 10^4$ year years on Europa.

Ion gun
Hydrogen ion
The dependence of the ion beam current on the electromagnetic coil current of the E × B filter was measured
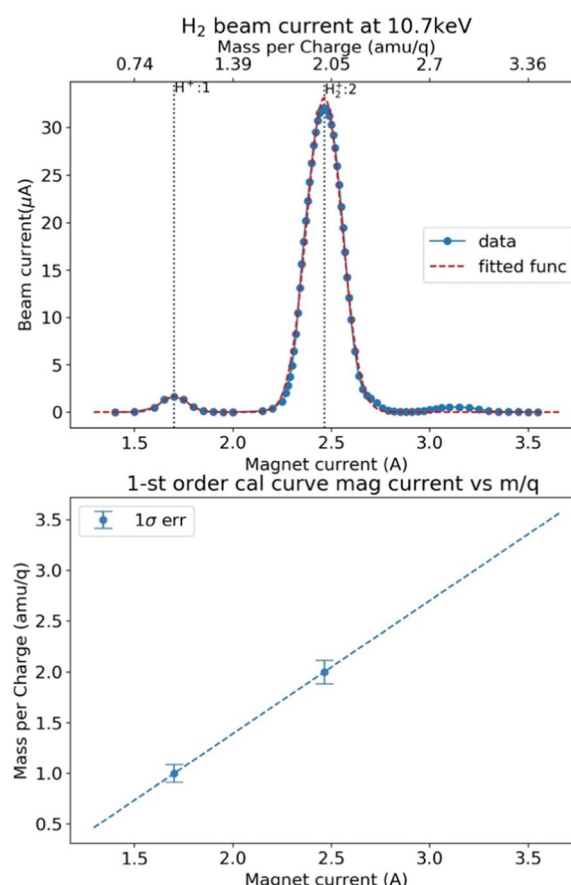

Fig. 7 Plots depicting the (top) ion beam current created from the hydrogen molecular gas with an acceleration voltage of 10.7 keV as a function of the E x B filter electromagnetic coil current and (bottom) the mass per charge of the incident ion as a linear function of the electromagnetic coil current. In the top panel, the blue dots connected with the blue line indicate the measured ion beam current in a unit of μA. The top horizontal axis shows the mass per charge calibrated with the linear function in the bottom panel. The red broken line is the sum of two Gaussian functions fitted to the measured beam current. In the bottom panel, the error bar shows the 1σ error estimated from the standard deviation of the fitted Gaussian functions. The blue broken line is the calibration line that associates the electromagnetic coil current with the mass per charge of the incident ion constrained with the H^+ and H_2^+ beam currents

for hydrogen, oxygen, carbon dioxide, and helium gases. The top panel of Fig. 7 shows the ion beam current created from hydrogen molecular gas with an acceleration voltage of 10.7 keV as a function of the E × B filter electromagnetic coil current. The two major peaks in the beam current correspond to the beams of the H^+ and H_2^+ ions. The electromagnetic coil current, width, and height of the current peaks were estimated by fitting Gaussian functions, as indicated by the red broken line in the top panel. From the height of the fitted function,

Kimura *et al. Earth, Planets and Space*   (2023) 75:150

Page 9 of 15

the H_2^+ ion beam current was found to have a greater value of 33.2 μA than that of the H_2^+ beam current of 1.70 μA The peaks of the two fitted Gaussian functions, 1.70 and 2.46 A in units of the electromagnetic coil current, correspond to the mass per charge ratios m/q for the H^+ and H_2^+ ions, 1 and 2 amu/q, respectively, where q is the incident ion charge in a unit of the elementary charge. The bottom panel of Fig. 7 shows a linear calibration function that associates the electromagnetic coil current with the mass per charge. The calibration function was constrained by the m/q ratios and the measured electromagnetic coil currents of H^+ and H_2^+. The standard deviations of the fitted Gaussian functions in the top panel of Fig. 7 correspond to those of m/q ratios for H^+ and H_2^+ on the calibration function, which are 0.086 and 0.12 amu/q, respectively. The estimated standard deviations are the resolutions of the mass per charge of each ionic species. These results demonstrate that the H^+ and H_2^+ ions are significantly resolved using the implemented $E \times B$ filter. With the obtained mass per charge resolution, the flux of the incident hydrogen is correctly estimated from the beam current measurement. The H_3^+ ion is also resolved with the $E \times B$ filter, which is likely detected as a minor bump around ~ 3 amu/q although its beam current is less significant ($< 1 \mu$A) compared to H^+ and H_2^+.

For example, the number and energy fluxes of the H_2^+ ion beam with a 10-mm diameter were estimated to be 5.23×10^{14} particles cm^{-2} s^{-1} and 2.82×10^{15} keV cm^{-2}s^{-1} from the measured beam current, which are equivalent to the number and energy fluences of 4.56×10^{19} particles cm^{-2} and 2.44×10^{20} keV cm^{-2} with a 1-day irradiation time in the experiment, respectively. Here, we estimated the number flux as the total flux of hydrogen atoms completely dissociated from the incident hydrogen molecule ion by collision with the target. The obtained number fluence satisfies the minimum system requirements ($> 10^{18}$ particles cm^{-2}) defined in "System requirements" section. With the number and energy fluxes (1.5×10^7 particles cm^{-2} s^{-1}) and (1.2×10^{10} keV cm^{-2}s^{-1}) of the keV–MeV hydrogen atom ions measured with the Galileo explorer in the orbit of Europa (Cooper et al. 2001), the estimated number and energy fluences correspond to irradiation times of 9.6×10^4 year and 6.4×10^2 years on Europa, respectively.

Oxygen ion

The ion beam current created from the oxygen molecular gas with an acceleration voltage of 10.7 keV is shown in Fig. 8 in the same format as Fig. 7. We found two ion current peaks of 3.18 and 14.9 μA at

the electromagnetic coil currents of 7.12 A (m/q = 16 amu/q) and 10.3 A (m/q = 32 amu/q), which correspond to O^+ and O_2^+, respectively. The mass per charge of O^+ was equivalent to that of O_2^{++}. The O_2^{++} ion was possibly created in the discharge chamber and extracted, but regarded as negligible here because other doubly charged ions were not confirmed in the present performance test, i.e., insufficient ionization potential energy for the doubly charged ions. Based on the Gaussian function fitting and calibration function for the mass per charge as done for the hydrogen ion beams, the m/q resolution was estimated to be 1.2 and 1.6 amu/q for the O^+ and O_2^+ ions, respectively.

For example, the number and energy fluxes of the O_2^+ ion beam with a 10 mm diameter were estimated to be 2.36×10^{14} particles cm^{-2} s^{-1} and
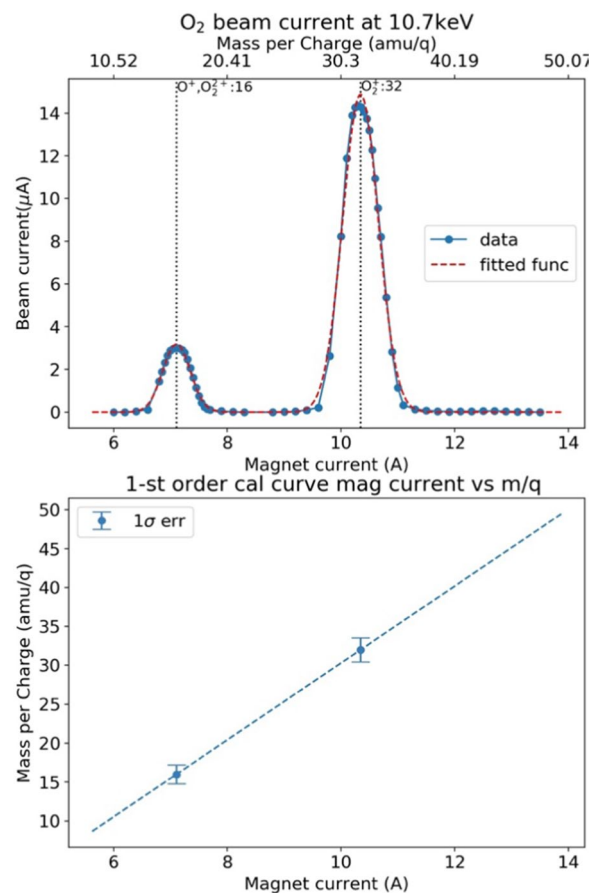

Fig. 8 Plots depicting the (top) ion beam current created from the oxygen molecular gas with an acceleration voltage of 10.7 keV as a function of the E x B filter electromagnetic coil current and (bottom) the mass per charge of the incident ion as a linear function of the electromagnetic coil current in the same formats as Fig. 7. The linear function in the bottom panel was constrained with the O^+ and O_2^+ ion beam currents

Kimura *et al. Earth, Planets and Space*   (2023) 75:150

Page 10 of 15

1.26×10^{15} keV cm^{-2} s^{-1} from the measured beam current, which are equivalent to the number and energy fluences of 2.04×10^{19} particles cm^{-2} and 1.09×10^{20} keV cm^{-2} with a 1-day irradiation time in the experiment, respectively. We estimated the number flux as the total flux of oxygen atoms completely dissociated from the incident oxygen molecule ion by collision with the target. The obtained number fluence satisfies the minimum system requirements ($> 10^{18}$ particles cm^{-2}) defined in "System requirements" Section. With the number and energy fluxes (1.5×10^6 particles cm^{-2} s^{-1}) and (1.8×10^9 keV cm^{-2}s^{-1}) of the keV–MeV oxygen atom ions measured with the Galileo explorer in the orbit of Europa (Cooper et al. 2001), the estimated number and energy fluences correspond to the irradiation times of 4.3×10^6 year and 1.9×10^3 years on Europa, respectively.

Carbon dioxide ion

The ion beam current created from the carbon dioxide molecule gas with an acceleration voltage of 10.7 keV measured is shown in Fig. 9 in the same format as Fig. 7. Four ion current peaks of 1.28, 2.38, 9.23, and 7.91 μA were found, which correspond to the C$^+$, O$^+$, CO$^+$, and CO$_2^+$ ions, respectively. As well as the oxygen ion current in "Oxygen ion" Section, the doubly charged ions, e.g., C^{++} and O^{++}, were not confirmed in the present performance test. The electromagnetic coil current of each ion species is 6.43 A (m/q$=12$ amu/q), 7.42 A (m/q$=16$ amu/q), 10.0 A (m/q$=28$ amu/q), and 12.6 A (m/q$=44$ amu/q), respectively. Based on the Gaussian function fitting and calibration function for the mass per charge as done for the hydrogen and oxygen ion beams, the m/q resolution was estimated to be $\sim 0.7, \sim 0.9, \sim 2$, and ~ 3 amu/q for C$^+$, O$^+$, CO$^+$, and CO$_2^+$, respectively. For example, the atomic number and energy fluxes of the CO$_2^+$ ion beam with a 10 mm diameter were estimated to be (1.89×10^{14} particles cm^{-2}s^{-1}) and (6.28×10^{14} keV cm^{-2} s^{-1}), which are equivalent to the number and energy fluences of (1.63×10^{19} particles cm^{-2}), and (5.43×10^{19} keV cm^{-2}), with a 1-day irradiation time in the experiment, respectively. Here, we estimated the number flux as the total flux of the carbon and oxygen atoms completely dissociated from the incident carbon dioxide molecule ion by collision with the target.

Other performances of ion gun

The ion beam created from helium atom gas with an acceleration voltage of 10.7 keV was also measured. The only ion created was the He$^+$ ion. An $E\times B$ filter was not used for the current measurements. The ion beam current was
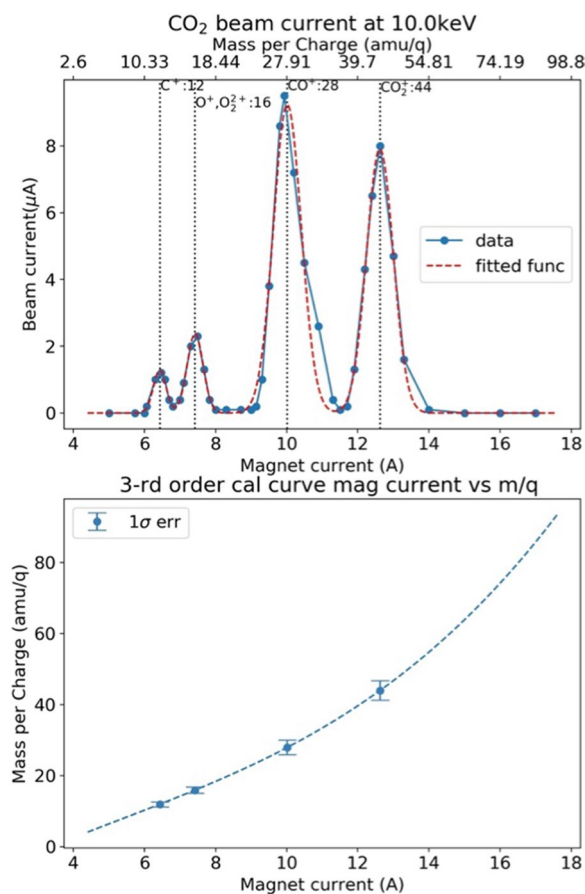

Fig. 9 Plots showing the (top) ion beam current created from the carbon dioxide molecular gas with an acceleration voltage of 10.0 keV as a function of the E x B filter electromagnetic coil current and (bottom) the mass per charge of the incident ion as a 3rd order polynomial function of the electromagnetic coil current in the same formats as Fig. 7. The polynomial function in the bottom panel was constrained by the C$^+$, O$^+$, CO$^+$, and CO$_2^+$ ion beam currents

27.0 μA. The current corresponds to the number and energy fluxes of (2.15×10^{14} particles cm^{-2} s^{-1}), and 2.30×10^{15} keV cm^{-2} s^{-1}, which are equivalent to the number and energy fluences of 1.85×10^{19} particles cm^{-2}, and 1.98×10^{20} keV cm^{-2}, with a 1-day irradiation time in the experiment, respectively. The results of the ion-beam current assessments are summarized in Table 2.

Furthermore, we assessed the magnetic field efficiency of the E$\times$B filter, which associates the theoretical magnetic flux density $B_0 = E_0/v$ with the measured flux B_{eff} as $B_{\text{eff}} = \varepsilon B_0$ (see "Ion gun with E x B filter" Section). B_0 and B_{eff} were obtained for each peak of the ion-beam current, as shown in Figs. 7, 8, 9. For example, for the H$_2^+$ ion beam, the theoretical B_0 was estimated to be 1018 G from the electric field E_0 and ion speed v while the measured B_{eff} was 730 G, which leads to an efficiency ε of 0.72.

Kimura *et al. Earth, Planets and Space*   (2023) 75:150

Page 11 of 15

Table 2 Summary of performance test for the ion gun with the E x B filter of the PIECE system

Gas	Particle	Energy (KeV)	Max beam current (μA)	m/q resol. (amu/q)[a]	B-field efficiency ε[b]	Number flux (#/cm$_2$/s)[c]	Energy flux (keV/cm$_2$/s)
–	Electron	$10.0 - 30.0$	$1.87 - 2.52 \times 10^3$	–	–	$1.49 - 2.00 \times 10^{16}$	$1.89 - 4.46 \times 10^{17}$
Hydrogen	H$^+$	10.7	1.70	1 ± 0.086	0.69	1.35×10^{13}	1.45×10^{14}
Hydrogen	H$_2^+$	10.7	33.2	2 ± 0.12	0.72	5.23×10^{14}	2.82×10^{15}
Helium	He$^+$	10.7	27.0			2.15×10^{14}	2.30×10^{15}
Oxygen	O$^+$, O$_2^{2+}$	10.7	3.18	16 ± 1.2	0.66	2.52×10^{13}	2.70×10^{14}
Oxygen	O$_2^+$	10.7	14.9	32 ± 1.6	0.68	2.36×10^{14}	1.26×10^{14}
Carbon dioxide	C$^+$	10.0	1.28	$12^{+0.70}_{-0.70}$	0.67	1.02×10^{13}	1.02×10^{14}
Carbon dioxide	O$^+$, O$_2^{2+}$	10.0	2.38	$16^{+0.93}_{-0.92}$	0.66	1.89×10^{13}	1.89×10^{14}
Carbon dioxide	CO$^+$	10.0	9.23	$28^{+2.1}_{-2.0}$	0.67	1.47×10^{14}	7.34×10^{14}
Carbon dioxide	CO^{2+}	10.0	7.91	$44^{+2.8}_{-2.6}$	0.67	1.89×10^{14}	6.28×10^{14}

[a] m/q resolution was estimated from the standard deviation of the Gaussian functions fitted to the beam current profile in Figs. 6, 7, 8

[b] B-field efficiency is the factor that associates the theoretical magnetic flux density in the $E \times B$ filter B_0 with the measured one B_{eff} as $B_{eff} = \varepsilon B_0$ (see details in "Ion gun with E x B filter"Sect.).

[c] The number fluxes for the polyatomic molecule ions (H$_2^+$, O$_2^+$, CO$^+$, CO^{2+}) were estimated as the total fluxes of the atoms completely dissociated from the incident molecule ions by collision with the target sample. The number fluxes of O$^+$ and O$_2^{++}$ were estimated by assuming that the contribution of O$_2^{++}$ was negligible

For the present $E \times B$ filter, the efficiency ε was found to range from 0.66 to 0.72.

The two-dimensional profile of the ion beam was assessed using a beam-profile monitor. For beam profile assessment, an ion gun with an $E \times B$ filter was located at a working distance of 160 mm from the profile monitor. Figure 10 shows an example of the 2D beam profile measured for the O$^+$ ions created from oxygen molecular gas. The current density was a normalized value in a unit of mm^{-2}. The x–y plane is perpendicular to the beam line, where the Faraday cup of the profile monitor (aperture diameter of 0.5 mm) was swept in the x- and y-axis directions. The sampling intervals are 1 mm and 0.002 mm for the x- and y-axes, respectively. The ion beam had a width of ~ 5.5 mm in the x-axis direction and ~ 3 mm in the y-axis direction. These widths are sufficiently narrow to irradiate a target sample with an 11 mm diameter. For the nominal system operation, this beam profile is going to be defocused to a 10 mm diameter.

Mass spectrometer

The partial pressure of each particle species in the main chamber was monitored using a QMS. We placed a pelletized NaCl target sample weighing ~ 0.2 g pelletized in a copper cup without irradiation. Figure 11 shows the measured partial pressure of each particle species as a function of atomic/molecular mass. The monitored pressures are the background of the particles degassing from the target sample and the inner wall of the main chamber. The background of each degassing particle species was temporally stable at an integration
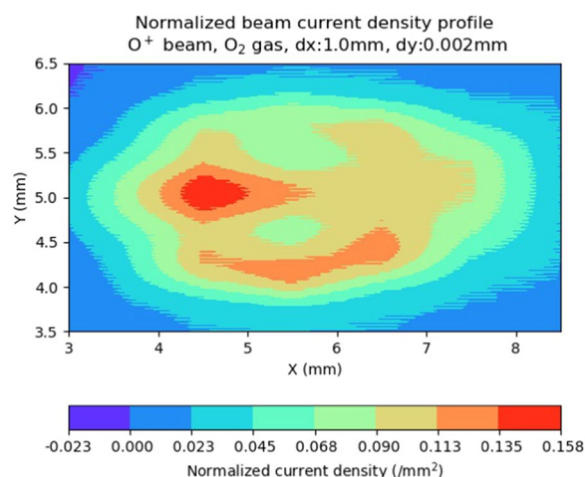

Fig. 10 Color contour plot illustrating an example of the two-dimensional profile of the ion beam current measured with the beam-profile monitor. The incident ion particle species is O$^+$ created from the oxygen molecular gas. The beam current was measured with the 0.5 mm aperture profile monitor swept at a spatial interval of 1 mm in the x-axis direction and 0.002 mm in the y-axis. The measured current density is normalized with the total current two-dimensionally integrated over the indicated x–y plane. The color contour indicates the normalized current density in a unit of mm^{-2} linearly interpolated between the x- and y-grids

time of 20 s, of which the mean and standard deviation were measured to be $\sim 10^{-7} - 10^{-6}$ Pa, and $\sim 10^{-8}$ Pa, respectively. Particles degassing from the target sample during irradiation are expected to be detected when the partial pressure of the particles is significantly greater than that of the standard deviation of $\sim 10^{-8}$ Pa, after subtracting the background. Table 3 summarizes the

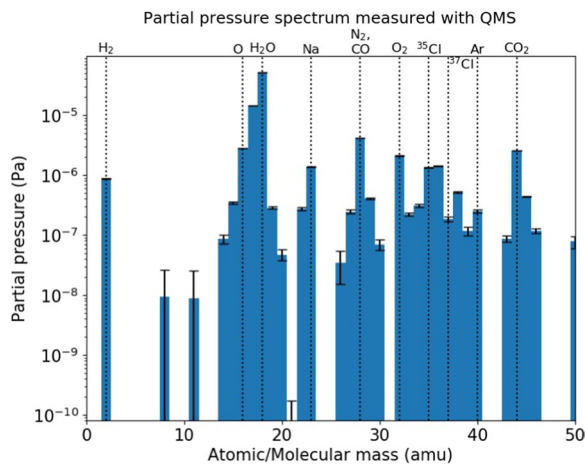Kimura *et al. Earth, Planets and Space*   (2023) 75:150

Page 12 of 15

Fig. 11 Bar graph showcasing the steady-state partial pressures of the atoms and molecules degassed from a NaCl target sample of 0.2 g and the inner wall of the main chamber measured with QMS as a function of the atomic/molecular mass. The blue bars show the partial pressure averaged over 20 s with the black error bars estimated from the standard deviation of the 20-s time series

Table 3 Average partial pressures and standard deviations measured in the steady state with QMS with an integration time of 20 s

Particle	Pressure (Pa)	Std. Dev. (Pa)
H_2	8.81×10^{-7}	1.15×10^{-8}
O	2.82×10^{-6}	1.01×10^{-8}
H_2O	5.15×10^{-5}	1.22×10^{-8}
Na	1.37×10^{-6}	1.94×10^{-8}
N_2, CO	4.15×10^{-6}	1.24×10^{-8}
O_2	2.11×10^{-6}	1.30×10^{-8}
^{35}Cl	1.32×10^{-6}	1.58×10^{-8}
^{37}Cl	1.85×10^{-7}	1.81×10^{-8}
Ar	2.52×10^{-7}	1.48×10^{-8}
CO_2	2.57×10^{-6}	1.23×10^{-8}

measured mean and standard deviation of the partial pressure for the major particle species confirmed in the present assessment.

The degassing rate of each particle species is estimated based on the ideal gas equation of state. Assuming that only the gas pressure p and number of gas particles N in the chamber are temporally variable, the time derivative of the equation of state is denoted as:

$$\frac{V}{p}\frac{\partial p}{\partial t} = \frac{RT}{p}\frac{\partial N}{\partial t} = \frac{RT\alpha}{p}, \tag{5}$$

where V is the internal volume of the chamber, R is the gas constant, T is the gas temperature, t is time, and $\alpha = \partial N/\partial t$ is the number of gas particles evacuated

from the chamber or degassed to the chamber per unit of time. α becomes negative or positive when evacuated or degassed, respectively. Equation 5 has the dimensions of the volume flow rate, which can be equated to $-A$ when no degassing occurs, where A is the pumping rate of the chamber. The number of gas particles evacuated per unit of time with no degassing α_0 is expressed as:

$$\alpha_0 = -\frac{Ap}{RT}. \tag{6}$$

In the steady state, when the gas pressure is temporally constant because of the balance between the evacuation and degassing, the time derivative of the pressure equals zero:

$$0 = \frac{\partial p}{\partial t} = \frac{RT}{V}(\alpha_0 + \alpha_d), \tag{7}$$

where α_d is the number of gas particles degassed from the target sample and/or inner chamber wall per unit of time. The degassing rate α_d is derived from Eqs. 6, 7 as follows:

$$\alpha_d = \frac{Ap}{RT}. \tag{8}$$

α_d is estimated from the measurable parameters A, p, R, and T for each degassing particle species. The degassing rate from the target sample $\alpha_{d,s}$ during the irradiation is estimated by subtracting the background rate $\alpha_{d,b}$ measured before the irradiation from the total degassing rate $\alpha_{d,i}$ measured during the irradiation, i.e., $\alpha_{d,s} = \alpha_{d,i} - \alpha_{d,b}$. This estimation should be applied to the temporally steady state of the gas pressure. The sputtering yield Y_s which is the number of particles sputtered from the target sample per incident particle, is related to the sample degassing rate $\alpha_{d,s}$ as follows:

$$Y_s = \frac{\alpha_{d,s}}{Sf_i}, \tag{9}$$

where S is the cross-section of the incident particle beam line focused on the sample surface and f_i is the number flux of the incident particle. Here, we assume that the degassed particles are sputtered only from the target sample and that the flux of the incident particle is temporally stable and spatially uniform. The detection sensitivities of the degassing rate and sputtering yield were estimated using Eqs. 8, 9. For example, with an incident oxygen atomic flux of 5.23×10^{14} particles cm^{-2} s^{-1}, by the O_2^+ ion and a 10-mm beam diameter, the detection sensitivities of $\alpha_{d,s}$ and Y_s for the sodium atom were estimated to be 2.59×10^{-12} mol s^{-1}, and 3.80×10^{-3} incident particle^{-1}, from the measured partial pressure sensitivity of 1.94×10^{-8} Pa, respectively.

Kimura *et al. Earth, Planets and Space*   (2023) 75:150

Page 13 of 15

Summary and future perspective

In this study, we successfully developed a plasma irradiation system for the exclusive use 'PIECE' that realistically reproduces surface space weathering of tenuous atmospheric bodies in our solar system. Characteristics of the developed electron gun were found to be as follows:

1. *Number fluence* $1.28 - 1.73 \times 10^{21}$ particles cm^{-2} at 10–30 keV with a 1-day irradiation time in the experiment.

2. *Energy fluence* $1.63 - 3.85 \times 10^{22}$ keV cm^{-2} at 10–30 keV with a 1 day irradiation time in the experiment.

3. *Irradiation time* the estimated number and energy fluences correspond to irradiation times of $2.3 - 3.0 \times 10^5$ and $0.84 - 2.0 \times 10^4$ years on Europa, respectively.

   Characteristics of the developed ion gun emitting multiple species of energetic ions (H^+, H_2^+, He^+, O^+, O_2^+, C^+, CO^+, and CO_2^+) were found to be as follows:

4. *m/q resolution* 0.086–2.8 amu/q at ∼ 10 keV.

5. *Number fluence*, e.g., $1.92 - 2.44 \times 10^{20}$ keV cm^{-2}, at ∼ 10 keV with a 1-day irradiation time in the experiment for the incident H_2^+ and O_2^+ ions.

6. *Energy fluence*, e.g., $1.92 - 2.44 \times 10^{20}$ keV cm^{-2}, at ∼ 10 keV with a 1-day irradiation time in the experiment for the incident H_2^+ and O_2^+ ions.

7. *Irradiation time*, e.g., the estimated number and energy fluences correspond to irradiation times of $0.96 - 43 \times 10^5$, and $6.4 - 19 \times 10^2$, years on Europa, respectively, in the experiment for the incident H_2^+ and O_2^+ ions.

   Based on the QMS measurements, detection characteristics for the degassing gas were found to be as follows:

8. *Pressure detection sensitivity* ∼ 10^{-8} Pa, for a background of ∼ $10^{-7} - 10^{-6}$ Pa,

9. *Degassing rate sensitivity* ∼ 10^{-12} mol s^{-1}.

As briefly introduced in "Introduction" and "System requirements" Sections, we apply the PIECE system to a variety of tenuous atmospheric bodies in our solar system to realistically reproduce plasma space weathering on their surfaces. The icy moons of the gas giants, which are Europa, Ganymede, Callisto, and Enceladus, are the highest-prioritized targets to uncover the chemical and physical evolution of the icy surface, which will characterize the chemical composition of the interior ocean. The irradiation of the potential surface sample materials, for example, ice and NaCl (Trumbo et al. 2019, 2022), with electrons, hydrogen, and oxygen (Thomas et al. 2004) using our system comprehensively models the icy surface alteration by Jovian magnetospheric plasma irradiation. Mercury, the Moon, and asteroids are also important targets to be addressed. The water molecular creation from their surface materials by solar wind irradiation (Jones et al. 2018, 2020) is reproduced by the irradiation of silicate mineral target samples with electrons and hydrogen, which also reproduces the creation of the exosphere by solar wind ion sputtering (Morrissey et al. 2022). The Moon and Phobos are continuously irradiated with the 'planetary winds', which comprised atmospheric particles escaping the planets. The accumulation of planetary wind particles on the surface of the moons is reproduced by the irradiation of silicate minerals with oxygen, hydrogen, and carbon dioxide (Ozima et al. 2005; Terada et al. 2009, 2017), which potentially reveals the evolution of atmospheric escape.

Author contributions

TK designed the system, wrote all the manuscript text, and prepared all the figures. TK, MO, TK, and RH integrated the system and made the system performance test. SH, RH, and TH fabricated the electron and ion guns implemented on the system and prepared the data for Figs. 8, 9. YN and FT supported the system design and provided the development budget. TT and AH supported experimental technology development. All authors reviewed the manuscript.

Availability of data and materials

The datasets used and/or analyzed during the current study are available from the corresponding author upon reasonable request.

Declarations

Competing interests

The authors declare that they have no competing interests.

Author details

[1]Department of Physics, Faculty of Science, Tokyo University of Science, 1-3 Kagurazaka, Shinjuku, Tokyo 162-8601, Japan. [2] Research Organization of Science and Technology, Ritsumeikan University, 1-1-1 Noji-higashi, Kusatsu, Shiga 525-8577, Japan. [3]Omegatron Co.Ltd., 2-22-12 Saikouchi, Hitachinaka, Ibaraki 312-0058, Japan. [4]Graduate School of Science, Tohoku University, 6-3 Aramaki, Aza Aoba, Aoba-ku, Sendai, Miyagi 980-8578, Japan. [5]RIKEN Nishina Center, 2-1 Hirosawa, Wako, Saitama 351-0198, Japan. [6]Space Technology Directorate I, Japan Aerospace Exploration Agency, Tsukuba Space Center, 2-1-1 Sengen, Tsukuba, Ibaraki 305-8505, Japan. [7]Department of Earth and Space Science, Osaka University, 1-1 Machikaneyama-cho, Toyonaka, Osaka 560-0043, Japan. [8]Graduate School of System Informatics, Kobe University, Kobe 657-8501, Japan. [9]Institute of Space and Astronautical Science, Japan Aerospace Exploration Agency, 3-1-1 Yoshinodai, Chuo-ku, Sagamihara, Kanagawa 252-5210, Japan.

Kimura *et al. Earth, Planets and Space*   (2023) 75:150

Page 14 of 15

References

Bennett CJ, Pirim C, Orlando TM (2013) Space-weathering of solar system bodies: a laboratory perspective. Chem Rev 113:9086–9150. https://doi.org/10.1021/cr400153k

Carlson RW, Calvin WM, Dalton JB, Hansen GB, Hudson RL, Johnson RE, McCord TB, Moore MH (2009) Europa's Surface Composition. University of Arizona Press, Tucson

Cooper JF, Johnson RE, Mauk BH, Garrett HB, Gehrels N (2001) Energetic Ion and electron irradiation of the Icy Galilean Satellites. Icarus 149:133–159. https://doi.org/10.1006/icar.2000.6498

Hand KP, Carlson RW (2015) Europa's surface color suggests an ocean rich with sodium chloride. Geophys Res Lett 42:3174–3178. https://doi.org/10.1002/2015gl063559

Helfenstein P, Shepard MK (1999) Submillimeter-scale topography of the lunar regolith. Icarus 141:107–131. https://doi.org/10.1006/icar.1999.6160

Ip W-H, Williams DJ, McEntire RW, Mauk BH (1998) Ion sputtering and surface erosion at Europa. Geophys Res Lett 25:829–832. https://doi.org/10.1029/98gl00472

Johnson RE (1990) Energetic charged-particle interactions with atmospheres and surfaces. Springer, Berlin

Johnson RE, Carlson RW, Cooper JF, Paranicas C, Moore MH, Wong MC (2004) Radiation effects on the surfaces of the Galilean satellites. In: Bagenal F, Dowling TE, McKinnon WB (eds) Jupiter. The Planet, Satellites and Magnetosphere, Cambridge

Jones BM, Alex Aleksandrov K, Hibbitts MD, Dyar TM (2018) Solar wind-induced water cycle on the moon. Geophys Res Lett 45(10959):10967. https://doi.org/10.1029/2018gl080008

Jones BM, Sarantos M, Orlando TM (2020) A new in situ quasi-continuous solar-wind source of molecular water on mercury. ApJL 891:L43. https://doi.org/10.3847/2041-8213/ab6bda

Laczniak DL, Thompson MS, Christoffersen R, Dukes CA, Clemett SJ, Morris RV, Keller LP (2021) Characterizing the spectral, microstructural, and chemical effects of solar wind irradiation on the Murchison carbonaceous chondrite through coordinated analyses. Icarus 364:114479. https://doi.org/10.1016/j.icarus.2021.114479

Madey TE, Yakshinskiy BV, Ageev VN, Johnson RE (1998) Desorption of alkali atoms and ions from oxide surfaces: relevance to origins of Na and K in atmospheres of mercury and the moon. J Geophys Res 103:5873–5887. https://doi.org/10.1029/98je00230

Mauk BH (2004) Energetic ion characteristics and neutral gas interactions in Jupiter's magnetosphere. J Geophys Res. https://doi.org/10.1029/2003ja010270

Moore MH, Hudson RL, Carlson RW (2007) The radiolysis of SO2 and H2S in water ice: Implications for the icy jovian satellites. Icarus 189:409–423. https://doi.org/10.1016/j.icarus.2007.01.018

Moroz LV, Starukhina LV, Rout SS, Sasaki S, Helbert J, Baither D, Bischoff A, Hiesinger H (2014) Space weathering of silicate regoliths with various FeO contents: New insights from laser irradiation experiments and theoretical spectral simulations. Icarus 235:187–206. https://doi.org/10.1016/j.icarus.2014.03.021

Morrissey LS, Tucker OJ, Killen RM, Nakhla S, Savin DW (2022) Solar wind ion sputtering of sodium from silicates using molecular dynamics calculations of surface binding energies. ApJL 925:L6. https://doi.org/10.3847/2041-8213/ac42d8

Nakauchi Y, Abe M, Ohtake M, Matsumoto T, Tsuchiyama A, Kitazato K, Yasuda K, Suzuki K, Nakata Y (2021) The formation of H2O and Si-OH by H2+ irradiation in major minerals of carbonaceous chondrites. Icarus 355:114140. https://doi.org/10.1016/j.icarus.2020.114140

Nash DB, Fanale FP (1977) Io's surface composition based on reflectance spectra of sulfur/salt mixtures and proton-irradiation experiments. Icarus 31:40–80

Nelson RM, Nash DB (1979) Spectral reflectance change and luminescence of selected salts during 2–10 KeV proton bombardment: Implications for Io. Icarus 39:277–285. https://doi.org/10.1016/0019-1035(79)90170-2

Nittler LR, Starr RD, Weider SZ, McCoy TJ, Boynton WV, Ebel DS, Ernst CM, Evans LG, Goldsten JO, Hamara DK, Lawrence DJ, McNutt RL Jr, Schlemm CE 2nd, Solomon SC, Sprague AL (2011) The major-element composition of Mercury's surface from MESSENGER X-ray spectrometry. Science 333:1847–1850. https://doi.org/10.1126/science.1211567

Ozima M, Seki K, Terada N, Miura YN, Podosek FA, Shinagawa H (2005) Terrestrial nitrogen and noble gases in lunar soils. Nature 436:655–659. https://doi.org/10.1038/nature03929

Pieters CM, Noble SK (2016) Space weathering on airless bodies. J Geophys Res Planets 121:1865–1884. https://doi.org/10.1002/2016JE005128

Poston MJ, Carlson RW, Hand KP (2017) Spectral behavior of irradiated sodium chloride crystals under Europa-like conditions. J Geophys Res Planets 122:2644–2654. https://doi.org/10.1002/2017je005429

Saito Y, Nishino MN, Fujimoto M, Yamamoto T, Yokota S, Tsunakawa H, Shibuya H, Matsushima M, Shimizu H, Takahashi F (2012) Simultaneous observation of the electron acceleration and ion deceleration over lunar magnetic anomalies. Earth Planets Space 64:83–92. https://doi.org/10.5047/eps.2011.07.011

Sasaki S, Nakamura K, Hamabe Y, Kurahashi E, Hiroi T (2001) Production of iron nanoparticles by laser irradiation in a simulation of lunar-like space weathering. Nature 410:555–557. https://doi.org/10.1038/35069013

Seki K, Hirahara M, Terasawa T, Mukai T, Saito Y, Machida S, Yamamoto T, Kokubun S (1998) Statistical properties and possible supply mechanisms of tailward cold O+beams in the lobe/mantle regions. J Geophys Res 103:4477–4489. https://doi.org/10.1029/97ja02137

Seki K, Elphic RC, Hirahara M, Terasawa T, Mukai T (2001) On atmospheric loss of oxygen ions from earth through magnetospheric processes. Science 291:1939–1941. https://doi.org/10.1126/science.1058913

Spencer JR, Tamppari LK, Martin TZ, Travis LD (1999) Temperatures on Europa from galileo photopolarimeter-radiometer: nighttime thermal anomalies. Science 284:1514–1516. https://doi.org/10.1126/science.284.5419.1514

Szalay JR, Smith HT, Zirnstein EJ, McComas DJ, Begley LJ, Bagenal F, Delamere PA, Wilson RJ, Valek PW, Poppe AR, Nénon Q, Allegrini F, Ebert RW, Bolton SJ (2022) Water-group pickup ions from Europa-genic neutrals orbiting Jupiter. Geophys Res Lett. https://doi.org/10.1029/2022gl098111

Terada N, Kulikov YN, Lammer H, Lichtenegger HIM, Tanaka T, Shinagawa H, Zhang T (2009) Atmosphere and water loss from early Mars under extreme solar wind and extreme ultraviolet conditions. Astrobiology 9:55–70. https://doi.org/10.1089/ast.2008.0250

Terada K, Yokota S, Saito Y, Kitamura N, Asamura K, Nishino MN (2017) Biogenic oxygen from Earth transported to the moon by a wind of magnetospheric ions. Nature Astronomy 1:0026. https://doi.org/10.1038/s41550-016-0026

Thomas N, Bagenal F, Hill TW, Wilson JK (2004) The Io neutral clouds and plasma torus Jupiter. Planet Satellites Magnetosphere 1:561

Tribbett PD, Loeffler MJ (2021) The sputtering of radiolytic O2 in ion irradiated H2O-ice. Surf Sci 707:121797. https://doi.org/10.1016/j.susc.2021.121797

Trumbo SK, Brown ME, Hand KP (2019) Sodium chloride on the surface of Europa. Sci Adv 5:eaaw7123. https://doi.org/10.1126/sciadv.aaw7123

Trumbo SK, Becker TM, Brown ME, Denman WTP, Molyneux P, Hendrix A, Retherford KD, Roth L, Alday J (2022) A New UV spectral feature on Europa: confirmation of NaCl in Leading-hemisphere Chaos Terrain. The Planet Sci J. https://doi.org/10.3847/PSJ/ac4580

Tsuchiyama A, Uesugi M, Matsushima T, Michikami T, Kadono T, Nakamura T, Uesugi K, Nakano T, Sandford SA, Noguchi R, Matsumoto T, Matsuno J, Nagano T, Imai Y, Takeuchi A, Suzuki Y, Ogami T, Katagiri J, Ebihara M, Ireland TR, Kitajima F, Nagao K, Naraoka H, Noguchi T, Okazaki R, Yurimoto H, Zolensky ME, Mukai T, Abe M, Yada T, Fujimura A, Yoshikawa M, Kawaguchi J (2011) Three-dimensional structure of Hayabusa samples: origin and evolution of Itokawa regolith. Science 333:1125–1128. https://doi.org/10.1126/science.1207807

Valek PW, Waite JH, Allegrini F, Ebert RW, Bagenal F, Bolton SJ, Connerney JEP, Kurth WS, Szalay JR, Wilson RJ (2022) In situ ion composition observations of Ganymede's outflowing ionosphere. Geophys Res Lett. https://doi.org/10.1029/2022gl100281

Kimura *et al. Earth, Planets and Space*   *(2023) 75:150*

Page 15 of 15

Zahnle K, Dones L, Levison HF (1998) Cratering rates on the Galilean satellites. Icarus 136:202–222. https://doi.org/10.1006/icar.1998.6015

Zhu C, Crandall PB, Gillis-Davis JJ, Ishii HA, Bradley JP, Corley LM, Kaiser RI (2019) Untangling the formation and liberation of water in the lunar regolith. Proc Natl Acad Sci USA 116:11165–11170. https://doi.org/10.1073/pnas.1819600116

Publisher's Note